# Non-Gaussian statistics of amide I mode frequency fluctuation of *N*-methylacetamide in methanol solution: Linear and nonlinear vibrational spectra

Cite as: J. Chem. Phys. **120**, 1477 (2004); https://doi.org/10.1063/1.1633549
Submitted: 18 September 2003 . Accepted: 21 October 2003 . Published Online: 13 January 2004

Kijeong Kwac, Hochan Lee, and Minhaeng Cho

# Non-Gaussian statistics of amide I mode frequency fluctuation of *N*-methylacetamide in methanol solution: Linear and nonlinear vibrational spectra

Kijeong Kwac, Hochan Lee, and Minhaeng Cho[a)]
*Department of Chemistry and Center for Multidimensional Spectroscopy, Division of Chemistry and Molecular Engineering, Korea University, Seoul 136-701, Korea*

(Received 18 September 2003; accepted 21 October 2003)

By carrying out molecular dynamics simulations of an *N*-methylacetamide (NMA) in methanol solution, the amide I mode frequency fluctuation and hydrogen bonding dynamics were theoretically investigated. Combining an extrapolation formula developed from systematic *ab initio* calculation studies of NMA–$(CH_3OH)_n$ clusters with a classical molecular dynamics simulation method, we were able to quantitatively describe the solvatochromic vibrational frequency shift induced by the hydrogen-bonding interaction between NMA and solvent methanol. It was found that the fluctuating amide I mode frequency distribution is notably non-Gaussian and it can be decomposed into two Gaussian peaks that are associated with two distinctively different solvation structures. The ensemble-average-calculated linear response function associated with the IR absorption is found to be oscillating, which is in turn related to the doublet amide I band shape. Numerically calculated infrared absorption spectra are directly compared with experiment and the agreement was found to be excellent. By using the Onsager's regression hypothesis, the rate constants of the interconversion process between the two solvation structures were obtained. Then, the nonlinear response functions associated with two-dimensional infrared pump–probe spectroscopy were simulated. The physics behind the two-dimensional line shape and origin of the cross peaks in the time-resolved pump–probe spectra is explained and the result is compared with 2D spectra experimentally measured recently by Woutersen *et al.* [S. Woutersen, Y. Mu, G. Stock, and P. Hamm, Chem. Phys. **266**, 137 (2001)]. © *2004 American Institute of Physics.* [DOI: 10.1063/1.1633549]

## I. INTRODUCTION

The peak shape and frequency of the amide I band has been found to be sensitively dependent on secondary structures of polypeptides and proteins.[1–30] Recently, as a novel tool for structure determination of polypeptides, a variety of two-dimensional (2D) vibrational spectroscopies have been experimentally used and theoretically proposed.[1–39] Among those applications of multidimensional coherent vibrational spectroscopies to various problems, it was shown that the 2D IR pump–probe spectroscopy can be used to directly probe solvation dynamics of amides. For instance, Zanni *et al.*[38] carried out 2D vibrational photon echo experiments of NMA dissolved in liquid water. Woutersen *et al.*[23] performed 2D IR pump–probe measurements of aqueous trialanine and NMA solutions and compared their results with molecular dynamics simulation studies to clarify the origins on the vibrational coupling and spectral evolution.

In this paper, we will present molecular dynamics simulation results on linear and nonlinear vibrational spectroscopies of the NMA-methanol solution. Eaton *et al.* carried out systematic IR absorption experiments for a few amide molecules in various polar and nonpolar solvents[40] and measured solvatochromic amide I mode frequency shift induced by the solute–solvent interaction. In particular, the amide I IR band of the NMA–methanol solution was observed to be the most peculiar one. In Fig. 1, the baseline-corrected amide I band of the NMA–methanol solution is plotted. Note that there are two peaks at 1660 and 1637 $cm^{-1}$. From the fact that the amide I mode frequency of an isolated NMA molecule is 1707 $cm^{-1}$,[41] the methanol solvent induces a strong redshift of the amide I mode frequency by $-47$ and $-70$ $cm^{-1}$ for the two peaks. Furthermore, the intensity of the high-frequency (1660 $cm^{-1}$) peak appears to be stronger than that of the low-frequency (1637 $cm^{-1}$) peak. In order to explain the nature of the doublet spectrum of the NMA–methanol solution, Eaton *et al.*[40] as well as Woutersen *et al.*[39] suggested that the doublet feature originates from heterogeneity of NMA–methanol solvation structures, i.e., two-species model. The carbonyl oxygen of an NMA molecule can form maximally two hydrogen bonds with protic solvent molecules like water and methanol. Therefore, Eaton *et al.* suggested that there would exist two different NMA–methanol configurations having either one or two hydrogen bonds with methanol molecules.[40] Consequently, they assigned the two peaks to these two different species. Later, as noted by Woutersen *et al.*,[39] the peak separation, which is about 20 $cm^{-1}$, is in good agreement with the *ab initio* calculation, where a single hydrogen-bond can shift the amide I mode frequency by about 20 $cm^{-1}$.[41] Furthermore, their molecular dynamics simulation results on the time evolution of the distance between O(NMA) atom and

a)Electronic mail: mcho@korea.ac.kr

 

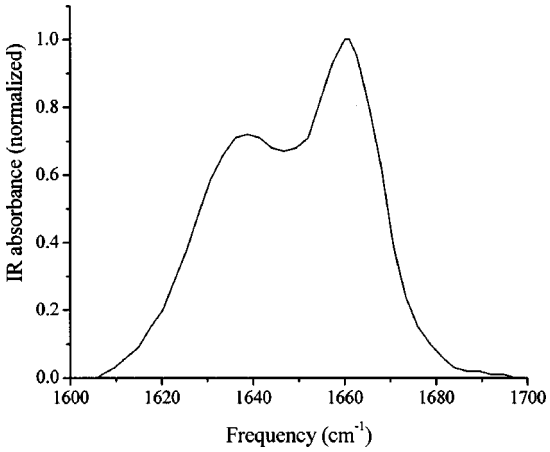


FIG. 1. The experimentally measured IR spectrum for NMA in methanol (this figure is taken from Ref. 40).

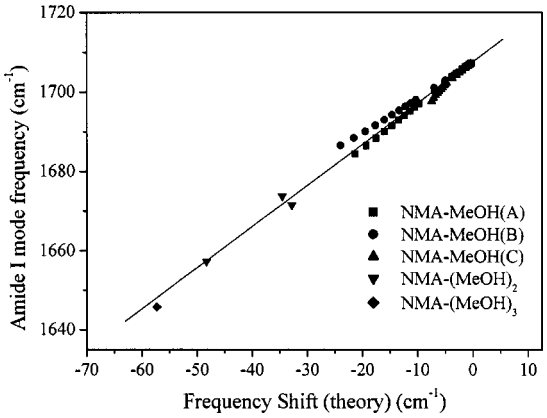


FIG. 2. Amide I mode frequency shifts for 66 NMA–MeOH complexes obtained by *ab initio* quantum chemistry calculations are plotted with respect to the theoretically predicted frequency shifts of amide I mode calculated by using the formula in Eq. (1) (see Ref. 41 for a detailed procedure).

hydroxyl D(methanol-$d_4$) atoms of three nearest methanol molecules supported the above interpretation using the two-species model.[39] However, due to the lack of theoretical model that is capable of quantitatively predicting solvatochromic amide I mode frequency shift and its fluctuation amplitude, their MD simulation results could not be used to quantitatively describe the amide I IR band as well as 2D IR pump–probe spectra.

In the present paper, we carried out both *ab initio* calculations of NMA–$(MeOH)_n$ clusters and MD simulation studies to elucidate the origin of this puzzling doublet feature. In Sec. II, we will use the extrapolation method that was developed in Ref. 41 and present various quantities specifying the band width and frequency redshift. In Sec. III, by using an ensemble averaging method for the calculation of the linear response function, numerically calculated IR absorption spectra of the NMA–MeOH solution will be presented and compared with experiment. In Sec. IV, numerically calculated nonlinear response functions associated with the 2D IR pump–probe spectroscopy will be presented and the time-evolution of the 2D IR pump–probe spectra will be compared with experimental results by Woutersen *et al.* in Ref. 39.

## II. MOLECULAR DYNAMICS SIMULATION: METHOD AND CORRELATION FUNCTION

### A. Extrapolation method

A spatially nonuniform electrostatic potential field created by the partial charges of surrounding solvent molecules can induce molecular structure distortion reflecting electronic structure change of the solute.[42] Recently, we developed the extrapolation method to quantitatively describe the amide I mode frequency shift of a hydrated NMA molecule. As shown in Ref. 41, the fluctuating amide I mode frequency is given by a linear curve in the six-dimensional space constructed by the electrostatic potential fields at the six NMA sites, i.e.,

$$\tilde{\nu}_I = \tilde{\nu}_I^0 + \delta\tilde{\nu}_I = \tilde{\nu}_I^0 + \sum_{a=1}^{6} l_a \phi_a , \tag{1}$$

where the six effective expansion coefficients, $l_a$, were given in Table I of Ref. 43. The electrostatic potential, $\phi_a$, is calculated by

$$\phi_a = \frac{1}{4\pi\epsilon_0} \sum_m \sum_j \frac{C_{j(m)}^{\mathrm{MeOH}}}{r_{aj(m)}}, \tag{2}$$

where $C_{j(m)}^{\mathrm{MeOH}}$ denotes the partial charge of the $j$th site of the $m$th methanol molecule and $r_{aj(m)}$ is the distance between the NMA site $a$ and the $j$th site of the $m$th methanol molecule. The methyl group in a methanol molecule will be treated as a united atom so that there are three partial charges producing spatially nonuniform electrostatic field around the NMA. In order to test the validity of this approach, we carried out *ab initio* geometry optimizations and vibrational analyses of various NMA–$(CH_3OH)_n$ (for $n=1-3$) clusters using the GAUSSIAN 98 program at the HF/6-311++G** level.[44] By using the six expansion coefficients, $l_a$, in Ref. 41, the theoretically predicted amide I mode frequencies of NMA–$(CH_3OH)_n$ clusters are compared with *ab initio* calculation results. In the present paper, we use rescaled coefficients, $l_a$, given in Ref. 43, and the three partial charges of $CH_3$, O, and H atoms of a methanol molecule in the AMBER program[45] are 0.2282, −0.6497, and $0.4215\,e$, where $e$ is the charge of an electron. As can be seen in Fig. 2, the agreement between the *ab initio* calculation results and theoretically predicted values with the above extrapolation formula, Eq. (1), is excellent.

### B. MD simulation method

In the present study, constant-energy molecular dynamics (MD) simulations of NMA in liquid methanol were performed by using the SANDER module of the AMBER program package employing the parm99 force field.[45] The simulated systems are a single NMA molecule dissolved in 259 methanol molecules in a cubic box with a periodic boundary condition. Long-range electrostatic interactions are treated by using the particle-mesh Ewald method[46] implemented in the AMBER. The system is minimized by 1000 steps of conjugate gradient method, and then they are equilibrated for 200 ps at

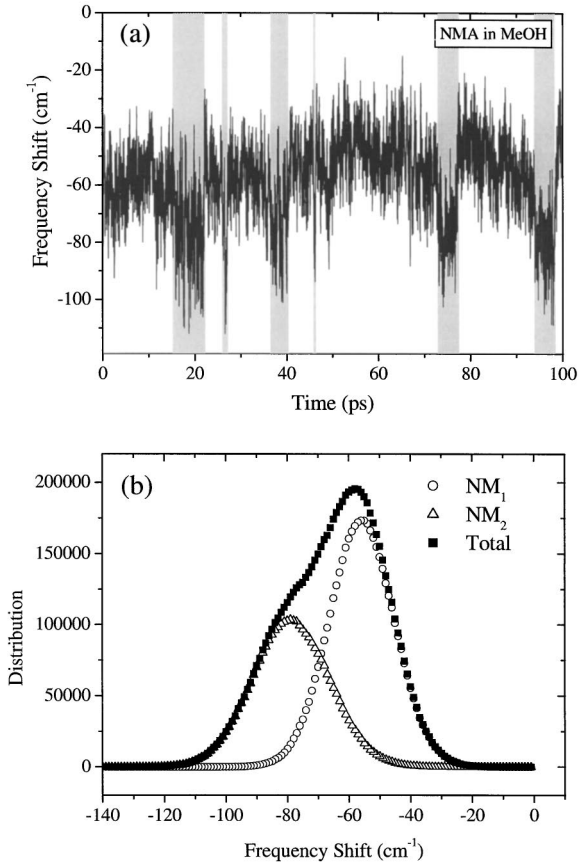


FIG. 3. (a) Time evolution of the fluctuating amide I mode frequency, $\delta\tilde{\nu}_I$, in cm$^{-1}$, which is calculated with Eq. (1) in combination with MD simulation. The shaded blocks correspond to the configurations where the carbonyl oxygen atom of the NMA forms simultaneous hydrogen bonds with two methanol molecules (see Fig. 4). (b) Distribution of the fluctuating amide I mode frequency, $\delta\tilde{\nu}_I$, calculated by using the formula in Eq. (1) (see closed squares). Also, the distributions of $\delta\tilde{\nu}_I$ from the MD configurations where the number of H-bonded methanol molecules to the C═O group are one (see open circles) and two (see open triangles) are plotted together.

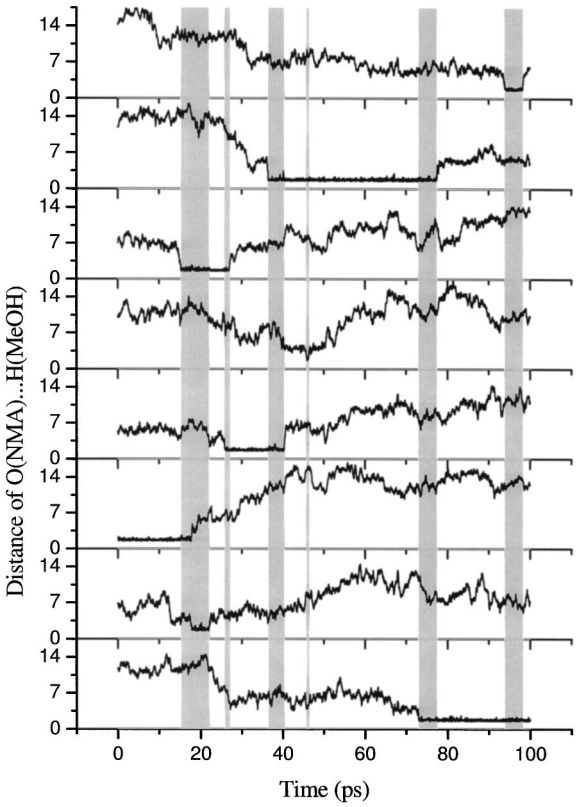


FIG. 4. Time evolutions of (NMA)O···H–O(MeOH) distances of eight methanol molecules that experience at least one direct hydrogen-bonding interaction with the NMA during the first 100 ps of the MD simulation trajectory. The shaded blocks correspond to the situation that two methanol molecules are directly hydrogen-bonded to the C═O group of the NMA.

298 K using the Berendsen coupling algorithm.[47] A time step of 0.5 fs was used and total simulation time was 4 ns.

### C. Amide I mode frequency fluctuation: Existence of two different solvation structures

The fluctuating amide I mode frequency shift, $\delta\tilde{\nu}_I(=\tilde{\nu}_I-\tilde{\nu}_I^0)$, given in Eq. (1) is plotted as a function of time in Fig. 3(a) and the distribution of $\delta\tilde{\nu}_I$ is shown in Fig. 3(b) (see the closed squares). Unlike the case of a NMA dissolved in liquid water, the shape of this distribution is strongly deviated from a Gaussian function. In order to study the physics behind this observation, we carefully examined the entire 4 ns trajectory and found that there are two distinctively different NMA–methanol solvation structures that can be distinguished from each other by the number of directly hydrogen-bonded methanol molecules to the carbonyl oxygen atom of the NMA. Here, the two H-bond criteria used are (1) (NMA)O···H(MeOH) distance is less than 2.5 Å and (2) (NMA)O···H–O(MeOH) angle is greater than 120°.[39]

Throughout this paper, we will refer those two different solvation configurations as

$$\text{Species } \mathrm{NM}_1 = \mathrm{NMA}\text{–}(\mathrm{MeOH})_1[\mathrm{MeOH}]_{N-1},$$

$$\text{Species } \mathrm{NM}_2 = \mathrm{NMA}\text{–}(\mathrm{MeOH})_2[\mathrm{MeOH}]_{N-2}.$$

In the above notation, $\mathrm{NMA}\text{–}(\mathrm{MeOH})_1[\mathrm{MeOH}]_{N-1}$, for example, means that the carbonyl oxygen atom of the NMA forms a direct hydrogen bond with a single methanol molecule. In order to clarify this division of the entire phase space into two regions, we plot the hydrogen-bond distance fluctuations in Fig. 4 for the first 100 ps trajectory. We found that only eight methanol molecules experience at least one direct hydrogen-bonding interaction with the carbonyl oxygen atom of the NMA. During the time periods emphasized by shaded blocks, the number of H-bonded methanol molecules to the C═O group are two. Otherwise, the number of H-bonds is one. This confirms that the explanations presented before by Eaton *et al.*[40] and Woutersen *et al.*[39] are basically correct, though Woutersen *et al.* suggested that the two different solvation configurations involve either one or zero H-bonded methanol molecule.[48] On the basis of this observation, we can divide the entire 4 ns trajectory into two parts (phase spaces) without any ambiguity, i.e., trajectories containing an NMA with a singly H-bonded methanol molecule and those with two H-bonded methanol molecules.

Now, for these two separated phase spaces, the $\delta\tilde{\nu}_I$ distributions of both $\mathrm{NM}_1$ and $\mathrm{NM}_2$ were calculated and plotted in Fig. 3(b) (open circles and open triangles, respectively). Each of the two distributions is well approximated to be a

Gaussian function, indicating that the amide I mode frequency fluctuation of $NM_1$ ($NM_2$) obeys a Gaussian statistics. The centers and widths of these two Gaussian-approximated peaks that are associated with $NM_1$ and $NM_2$ are $-55.9$, 21, $-78.9$, and 25 $cm^{-1}$, respectively. Conclusively, the existence of two solvation structures explains why the distribution of fluctuating amide I mode frequency deviates from a single Gaussian function. Furthermore, from the areas of the two Gaussian peaks in Fig. 3(b), we found that the mole fractions of $NM_1$ and $NM_2$ are 0.6 and 0.4, respectively.

In addition to the C═O group, the N–H group is also the other H-bonding site. On the basis of the MD trajectory analysis, we found that the H atom of the N–H group forms an H-bond to the oxygen atom of a methanol molecule for 80% of the total MD run times. However, as found before,[41] the H-bonding interaction of N–H···O(methanol) does not strongly affect on the amide I frequency redshift so that the asymmetric (non-Gaussian) distribution of the amide I mode frequency is not related to the presence of the N–H···O(methanol) H-bond.

In contrast to the NMA–methanol solution studied in the present paper, the fluctuating amide I mode frequency distribution of an *aqueous* NMA solution was found to be a single Gaussian function.[43] Then, a question immediately raised is how the hydrogen-bonding interactions in the NMA–methanol differ from those in the NMA–water system. Note that both a single water and a methanol molecule can form an equally strong H-bond to the C═O group. However, when a single H-atom in a water molecule, which is not directly involved in an H-bonding interaction with the NMA, is replaced with a methyl group in methanol, the latter group will occupy slightly larger volume in the first solvation shell. Thus, an additional H-bond by the second methanol molecule can be formed only after overcoming an excluded volume barrier, whereas there is no such barrier in the case of the NMA–water system. Due to this difference and influence of the excluded volume effect, the relative population of $NM_2$ conformation is as small as 40%—note that, in the case of an aqueous NMA solution, the carbonyl oxygen atom of the NMA is fully H-bonded to two water molecules.

Before we close this subsection, we will discuss a few more observations on equilibrium (statistical) properties. From Fig. 3(b), we calculated the ensemble averaged frequency shifts, $\langle \delta\tilde{\nu}_I \rangle$, for the NMA in liquid methanol, which is estimated to be $-64.6$ $cm^{-1}$. Eaton *et al.* reported that the solvatochromic amide I mode frequency shift by the MeOH solvent is about $-56$ $cm^{-1}$, which is the average of the two redshifted peaks.[40] The agreement between theory and experiment is acceptable. For the sake of completeness and comparison with future works on this system, the second and third moments are calculated and found to be $\langle (\delta\tilde{\nu}_I - \langle \delta\tilde{\nu}_I \rangle)^2 \rangle = 286\,cm^{-2}$ and $\langle (\delta\tilde{\nu}_I - \langle \delta\tilde{\nu}_I \rangle)^3 \rangle = -895\,cm^{-3}$, respectively. As will be shown in the following sections, due to this non-Gaussian statistics of the amide I mode frequency fluctuation, one cannot directly use the so-called second-order truncated cumulant expansion technique[49] to calculate the linear and nonlinear response functions.

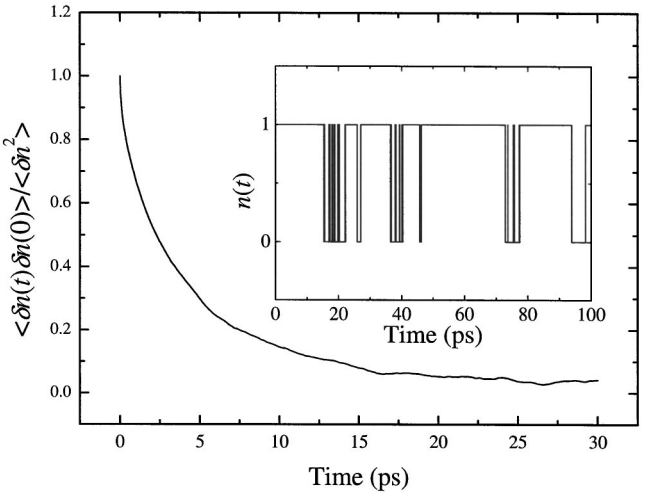


FIG. 5. The normalized equilibrium correlation function of $n(t)$, the left-hand side of Eq. (6). In the inset, $n(t)$ is plotted for the first 100 ps.

### D. Kinetics

As shown in the above subsection, the two species, $NM_1$ and $NM_2$, are in equilibrium and the rate equations can be deduced by assuming the following equilibrium reaction:

$$NM_1 \underset{k_b}{\overset{k_f}{\rightleftharpoons}} NM_2. \tag{3}$$

The forward and backward rate constants were denoted as $k_f$ and $k_b$, respectively. From the relative populations (mole fractions) of the two species, the equilibrium constant was found to be

$$K_{eq} = \frac{k_f}{k_b} = \frac{2}{3}. \tag{4}$$

The rate equations are written as

$$\frac{d}{dt}\begin{pmatrix} [NM_1]_t \\ [NM_2]_t \end{pmatrix} = \begin{pmatrix} -k_f & k_b \\ k_f & -k_b \end{pmatrix}\begin{pmatrix} [NM_1]_t \\ [NM_2]_t \end{pmatrix}. \tag{5}$$

In order to determine the two rate constants, we should first define the dynamical variable $n(t)$ for which

$n(t)=1$, if the solvated NMA structure belongs to $NM_1$ configuration at time $t$;

$n(t)=0$, if the solvated NMA structure belongs to $NM_2$ configuration at time $t$.

Note that $\langle n \rangle$ equals to the mole fraction of $NM_1$. Then, from the fluctuation-dissipation theorem (or Onsager regression hypothesis), we have[50]

$$\frac{\langle n(t)n(0)\rangle - \langle n\rangle^2}{\langle n\rangle(1-\langle n\rangle)} = \exp(-t/\tau_{rxn}), \tag{6}$$

where

$$\tau_{rxn} = \frac{1}{k_f + k_b}. \tag{7}$$

In the inset of Fig. 5, the trajectory of $n(t)$ is plotted for the

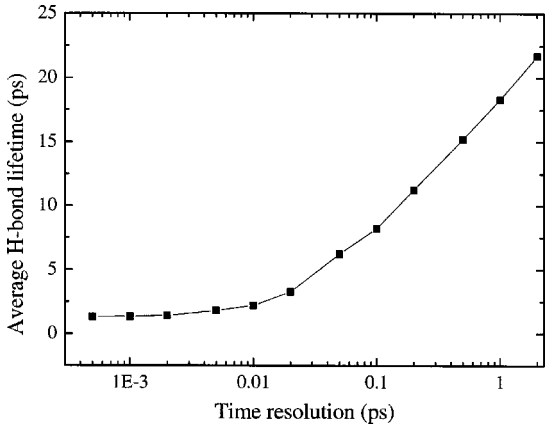


FIG. 6. The average hydrogen-bond lifetime $\langle\tau\rangle$ is calculated as a function of the time resolution used.

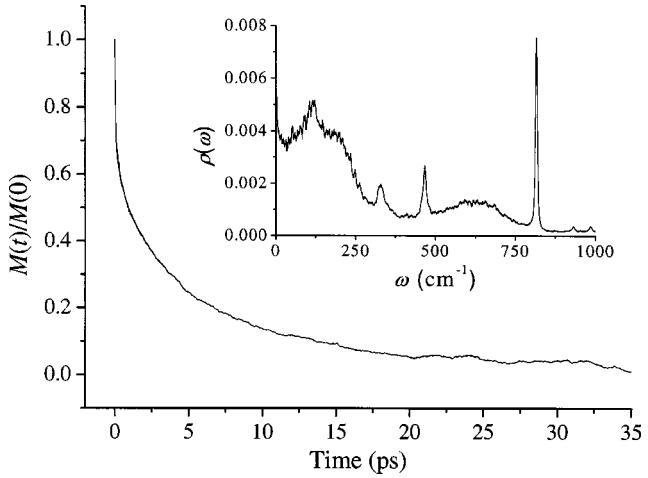


FIG. 7. The normalized $M(t)$. In the inset, the spectral distribution function, $\rho(\omega)$ defined in Eq. (9), is plotted.

first 100 ps, and the left-hand side of Eq. (6) is plotted in Fig. 5. From an exponential fit with Eq. (4), we found that the two rate constants are, respectively,

$$k_f = 0.068 \ \text{ps}^{-1}, \qquad k_b = 0.102 \ \text{ps}^{-1}. \tag{8}$$

We will use these rate constants to numerically calculate 2D vibrational spectra of the NMA–methanol solution.

### E. Hydrogen bond lifetime

As can be seen in the MD trajectory of the O···H bond distance in Fig. 4, the carbonyl oxygen atom can form either one or two hydrogen bonds with solvent methanol. From the entire trajectories of O(NMA)···H(MeOH) bond distances of each individual methanol molecule, one can directly calculate the average H-bond lifetime, $\langle\tau\rangle$. Here, it should be emphasized that the H-bond lifetime is critically dependent on the definition (criteria) of the H-bond as well as on the time resolution. Woutersen *et al.*[39] assumed that the time resolution for H-bond lifetime calculation is 2 ps, which means that if a methanol molecule form a single H-bond with the NMA over the 2 ps time window, regardless of the number of H-bond breaking and formation processes, it is counted as a single continuous H-bond. However, we found that the H-bond breaking and rearrangement occur very fast so that the 2 ps time resolution may not be short enough to capture the ultrafast H-bonding dynamics and overestimates the H-bond lifetime. In order to systematically study this time-resolution dependence of the calculated H-bond lifetime, in Fig. 6 $\langle\tau\rangle$ is plotted as a function of time resolution (width of the time window). Depending on the time resolution varying from 1 fs to 2 ps, the estimated H-bond lifetime varies from 1.3 ps to 22 ps. It is interesting to note that the average H-bond lifetime does not vary much when the time resolution is in between 1 fs to 10 fs. We used and will use the time resolution of 5 fs throughout this paper, which was also used in the kinetics analysis given in Sec. II D. In the 2 ps time resolution used by Woutersen *et al.* in Ref. 39, our estimated H-bond lifetime of 22 ps is a bit larger than their value of ~12 ps, which was obtained by using the GROMOS program.[39]

### F. $M(t)$ and pure vibrational dephasing constants

In order to investigate the time-correlation property of $\delta\tilde{\nu}_I(t)$, the autocorrelation function, $M(t)$, of $\delta\tilde{\nu}_I(t)$ is calculated, where $M(t)$ is defined as $M(t) = \langle \delta\omega_{10}(t)\,\delta\omega_{10}(0)\rangle$ and $\delta\omega_{10}(t) = \omega_{10}(t) - \langle\omega_{10}\rangle = 2\pi c\{\delta\tilde{\nu}_I(t) - \langle\delta\tilde{\nu}_I\rangle\}$. $M(t)$ plotted in Fig. 7 exhibits a bimodal decaying pattern and the slowly decaying part of $M(t)$ is almost an exponential function. However, unlike the case of the aqueous NMA solution, where the distribution of $\delta\tilde{\nu}_I(t)$ is a perfect Gaussian function, the fluctuation of $\delta\tilde{\nu}_I(t)$ in NMA–methanol solution is non-Gaussian so that the cumulant expansion approximation cannot be used to numerically simulate linear and nonlinear vibrational spectra as will be demonstrated in Sec. III. Therefore, the linear correlation function $M(t)$ does not play a crucial role in the present case. Nevertheless, for the sake of comparison with the case of NMA–water solution, we shall present a theoretical analysis using the so-called generalized Kubo model recently discussed by Schmidt, Sundlass, and Skinner in Ref. 52, where the frequency fluctuation correlation function was assumed to be a weighted sum of two exponential functions. That is to say, $M(t)$ in Fig. 7 is approximately written as $M(t) = \Delta_1^2 e^{-t/\tau_1} + \Delta_2^2 e^{-t/\tau_2}$, where the relaxation times $\tau_1$ and $\tau_2$ represent the two timescales for frequency fluctuations. By fitting the above formula to $M(t)$, we found that the relaxation times and their amplitudes are $\Delta_1^2 = 3.31\,\text{ps}^{-2}$, $\tau_1 = 0.12$ ps, $\Delta_2^2 = 5.37\,\text{ps}^{-2}$, and $\tau_2 = 4.38$ ps. These values give $\Delta_1\tau_1 = 0.22$ and $\Delta_2\tau_2 = 10.1$ so that the fast and slow processes satisfy their respective requirements for homogeneous and inhomogeneous broadenings, respectively. In particular, it is believed that the slowly decaying component of $M(t)$ is mainly due to the interconversion transitions between the two species, $NM_1$ and $NM_2$, considering the fact that $\tau_{\text{rxn}}$ given in Eq. (7) is 5.8 ps, which is close to the value of $\tau_2$.

### G. Distribution of coupled bath modes

The frequency distribution of the bath modes giving rise to decaying of $M(t)$ can be obtained by Fourier transforming the normalized $M(t)$ and the relevant spectral distribution function $\rho(\omega)$ is defined as[43]

$$\rho(\omega) \equiv 2 \tanh(\hbar\omega/2k_BT) \int_0^\infty dt \cos(\omega t)\{M(t)/M(0)\}, \tag{9}$$

which is plotted in Fig. 7 (see the inset). Here, $k_B$ and $T$ are the Boltzmann constant and temperature, respectively. In comparison to that of the NMA–water system,[43] there are no high frequency ($>750$ cm$^{-1}$) solvent modes in this case. Nevertheless, the three intramolecular NMA modes found in the NMA–water system[43] also appear in the spectral distribution, $\rho(\omega)$, at 330, 460, and 817 cm$^{-1}$, though they make negligible contributions to the shape and intensity of linear and nonlinear vibrational spectra.

## III. IR ABSORPTION SPECTRUM: LINEAR SPECTROSCOPY

The absorption line shape function is given by the Fourier transform of the quantum mechanical dipole correlation function as[51]

$$I(\omega) \sim \int_{-\infty}^{\infty} dt e^{i\omega t} \langle \boldsymbol{\mu}(t) \cdot \boldsymbol{\mu}(0) \rangle, \tag{10}$$

where $\boldsymbol{\mu}$ denotes the quantum mechanical dipole operator. $I(\omega)$ can be rewritten as, in terms of the linear response function $J(t)$,

$$I(\omega) \sim \int_{-\infty}^{\infty} dt e^{i\omega t} \overline{J}(t), \tag{11}$$

where $\overline{J}(t) = J(t)\exp(-i\langle\omega_{10}\rangle t)$ and

$$J(t) \equiv \left\langle \exp_+ \left[ -i \int_0^t d\tau \delta\hat{\omega}_{10}(\tau) \right] \right\rangle. \tag{12}$$

Here, $\delta\hat{\omega}_{10}(\tau)$ is the fluctuating angular frequency operator in the Heisenberg representation. $\langle \cdots \rangle$ is, in this case, the quantum mechanical trace over the bath eigenstates.

### A. Amide I IR band: Ensemble averaging (method 1)

As shown in Sec. II C, the amide I mode frequency fluctuation in the NMA–methanol solution is non-Gaussian so that one cannot directly use the second-order truncated cumulant expansion technique to calculate the linear response function, $J(t)$—note that the dashed–dotted curve in Fig. 8(b) is $I(\omega)$ calculated by using the second-order cumulant expansion method and at first sight it differs from the experimental result of Fig. 1. Therefore, we instead use a classical ensemble averaging method in the present subsection, and yet another method will be discussed in the following subsection. The linear response function in Eq. (12) is approximated as

$$J_c(t) = \left\langle \exp \left[ -i \int_0^t d\tau \delta\omega_{10}(\mathbf{q},\mathbf{p},\tau) \right] \right\rangle; \tag{13}$$

where the fluctuating part of the amide I mode frequency, $\delta\hat{\omega}_{10}(\tau)$, was replaced with a classical function, $\delta\omega_{10}(\mathbf{q},\mathbf{p},\tau)$, in the phase space of the bath and the average transition frequency $\langle\omega_{10}\rangle$ is also calculated over the classical ensemble. From the MD trajectories, one can evaluate $J_c(t)$ directly and the real and imaginary parts of $J_c(t)$ are plotted in Fig. 8(a). It is interesting to note that the real part of $J_c(t)$ is an oscillating function like an underdamped harmonic oscillator and also that the imaginary part of $J_c(t)$ is not negligibly small. Using Eq. (11), we can rewrite $I(\omega)$ as

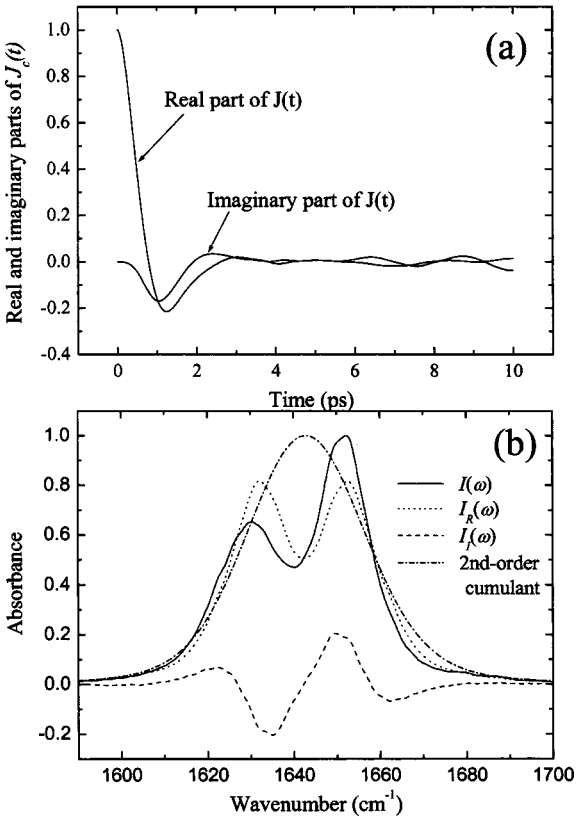


FIG. 8. (a) The real and imaginary parts of $J_c(t)$ defined in Eq. (13) are plotted. (b) The IR absorption line shape, $I(\omega)$, and its two contributions, $I_R(\omega)$ and $I_I(\omega)$ defined in Eq. (15), are plotted. Here the lifetime broadening effect was taken into account by using Eq. (16). Also, the absorption line shape calculated by the second-order cumulant expansion method (Ref. 43) is plotted for the sake of comparison.

$$I(\omega) = I_R(\omega) + I_I(\omega), \tag{14}$$

where the two contributions, $I_R(\omega)$ and $I_I(\omega)$, associated with the real and imaginary parts of $J_c(t)$ are defined as

$$\begin{aligned} I_R(\omega) &= \int_0^\infty dt \cos\{(\omega - \langle\omega_{10}\rangle)t\} \mathrm{Re}[J_c(t)], \\ I_I(\omega) &= -\int_0^\infty dt \sin\{(\omega - \langle\omega_{10}\rangle)t\} \mathrm{Im}[J_c(t)]. \end{aligned} \tag{15}$$

In Fig. 8(b), $I_R(\omega)$, $I_I(\omega)$, and $I(\omega)$ are plotted. Here, the lifetime broadening effect was taken into account by using the following ad hoc approximation:

$$J_c(t) \rightarrow J_c(t)\exp(-t/2T_1), \tag{16}$$

where the lifetime of the first excited state was assumed to be 1.8 ps.[39] The absorption spectrum $I(\omega)$ appears to be a doublet. Note that $I_R(\omega)$ spectrum is doublet and symmetric, whereas $I_I(\omega)$ is asymmetric. On the basis of these observations, we found that the oscillating behavior of $\mathrm{Re}[J_c(t)]$ is responsible for the doublet feature of the amide I band of the NMA–methanol solution. Also, the difference of the two

peak intensities originates from the nonzero $\mathrm{Im}[J_c(t)]$. Although the numerically calculated $I(\omega)$ are very close to the experimentally measured spectrum shown in Fig. 1, the interpretation given above might appear to be puzzling. In the following subsection we will present a detailed discussion and underlying physics behind these observations.

### B. Amide I IR band: Two-species model (method 2)

Instead of considering the entire phase space, as mentioned in Sec. II one can divide it into two phase spaces, where the two are separated by a potential barrier between $\mathrm{NM}_1$ and $\mathrm{NM}_2$. When the potential barrier is sufficiently high so that the time scales of motion within each of the two separated phase spaces are separated from the time scales of barrier crossings, one can ignore dynamic correlations between the two species. In this limit, the linear response function can be approximately written as a sum of two terms as

$$\bar{J}(t) = X_{\mathrm{NM}_1}\bar{J}_1(t) + X_{\mathrm{NM}_2}\bar{J}_2(t) = 0.6\bar{J}_1(t) + 0.4\bar{J}_2(t), \tag{17}$$

where $X_{\mathrm{NM}_1}$ and $X_{\mathrm{NM}_2}$ are mole fractions of $\mathrm{NM}_1$ and $\mathrm{NM}_2$, respectively, and

$$\begin{aligned}\bar{J}_1(t) &= \exp(-i\langle\omega_{10}\rangle_{\mathrm{NM}_1}t) \\ &\quad\times\left\langle \exp_+\left[-i\int_0^t d\tau\,\delta\hat{\omega}_{10}(\tau)\right]\right\rangle_{\mathrm{NM}_1}, \\ \bar{J}_2(t) &= \exp(-i\langle\omega_{10}\rangle_{\mathrm{NM}_2}t) \\ &\quad\times\left\langle \exp_+\left[-i\int_0^t d\tau\,\delta\hat{\omega}_{10}(\tau)\right]\right\rangle_{\mathrm{NM}_2}.\end{aligned} \tag{18}$$

Here the average over the $\mathrm{NM}_1$ ($\mathrm{NM}_2$) phase space was denoted as $\langle\cdots\rangle_{\mathrm{NM}_1}$ ($\langle\cdots\rangle_{\mathrm{NM}_2}$). As can be seen in Fig. 3(b), each amide I mode frequency distribution associated with either $\mathrm{NM}_1$ or $\mathrm{NM}_2$ phase space is a Gaussian function so that the cumulant expansion method with proper semiclassical approximations discussed in Ref. 43 can be directly used to calculate the $J_1(t)$ and $J_2(t)$. Then, we have

$$\begin{aligned}\bar{J}_1(t) &= \exp(-i\langle\omega_{10}\rangle_{\mathrm{NM}_1}t - g_1(t)), \\ \bar{J}_2(t) &= \exp(-i\langle\omega_{10}\rangle_{\mathrm{NM}_2}t - g_2(t)),\end{aligned} \tag{19}$$

where

$$\begin{aligned}g_1(t) &\equiv \int_0^t d\tau_2\int_0^{\tau_2} d\tau_1\langle\delta\omega_{10}(\tau_1)\,\delta\omega_{10}(0)\rangle_{\mathrm{NM}_1}, \\ g_2(t) &\equiv \int_0^t d\tau_2\int_0^{\tau_2} d\tau_1\langle\delta\omega_{10}(\tau_1)\,\delta\omega_{10}(0)\rangle_{\mathrm{NM}_2}.\end{aligned} \tag{20}$$

A detailed discussion on how to calculate the line-shape functions, $g_1(t)$ and $g_2(t)$, from the classical MD simulation was presented in Ref. 43. In Fig. 9(a), the two classical correlation functions, $M_1(t) = \langle\delta\omega_{10}(t)\,\delta\omega_{10}(0)\rangle_{\mathrm{NM}_1}$ and $M_2(t) = \langle\delta\omega_{10}(t)\,\delta\omega_{10}(0)\rangle_{\mathrm{NM}_2}$, that are amide I mode frequency fluctuation autocorrelation functions of $\mathrm{NM}_1$ and $\mathrm{NM}_2$ species, respectively, are plotted. Note that the two correlation functions exhibit the same bimodal decaying pattern and the mean square fluctuation amplitude of the $\mathrm{NM}_2$ amide I frequency fluctuation is larger than that of $\mathrm{NM}_1$, which indicates that the line shape of the $\mathrm{NM}_2$ species is broader than that of the $\mathrm{NM}_1$ species. In Fig. 9(a), the normalized correlation function, $M(t)/M(0)$ shown in Fig. 7, is also plotted for the sake of comparison. It is observed that $M(t)/M(0)$ decays much more slowly than $M_1(t)/M_1(0)$ or $M_2(t)/M_2(0)$ does. This can be easily understood by noting that the phase space considered in the calculation of $M(t)$ is much wide and involves conformational inhomogeneity of the solvation structures. That is to say, the slowly decaying part of $M(t)$ is related to the conformational transition processes (equilibrium reaction dynamics) between $\mathrm{NM}_1$ and $\mathrm{NM}_2$. Now, the two IR absorption spectra, $I_{\mathrm{NM}_1}(\omega)$ and $I_{\mathrm{NM}_2}(\omega)$, obtained by Fourier transforming $X_{\mathrm{NM}_1}\bar{J}_1(t)$ and $X_{\mathrm{NM}_2}\bar{J}_2(t)$ are plotted in Fig. 9(b), and in the same figure the total absorption spectrum is also shown as a solid curve. This resultant $I(\omega)$ can now be directly compared with the spectrum calculated by using the so-called classical ensemble averaging method [see the solid curve in Fig. 8(b)]. The two curves are in good agreement with each other, which means that the two-species model with cumulant expansion tech-

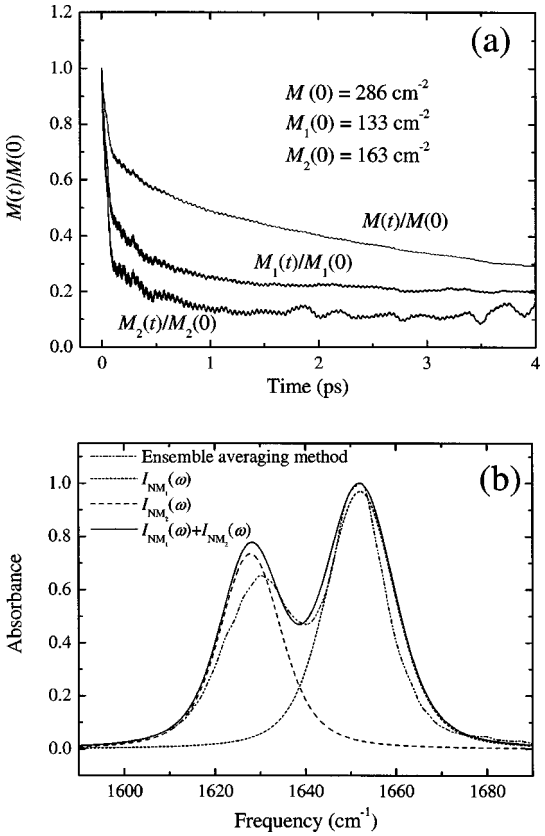


FIG. 9. The two classical correlation functions, $M_1(t)$ and $M_2(t)$, which are amide I mode frequency fluctuation autocorrelation functions of the $\mathrm{NM}_1$ and $\mathrm{NM}_2$ species, respectively, are plotted together with the normalized $M(t)$ shown in Fig. 7. The two IR absorption spectra, $I_{\mathrm{NM}_1}(\omega)$ and $I_{\mathrm{NM}_2}(\omega)$, obtained by Fourier transforming $X_{\mathrm{NM}_1}\bar{J}_1(t)$ and $X_{\mathrm{NM}_2}\bar{J}_2(t)$, respectively, are plotted with their sum. The IR absorption spectrum of Fig. 8(b) obtained by the ensemble averaging calculation is also plotted for comparison.

niques separately used to calculate absorption spectra of the two species is quantitatively reliable for the calculation of the amide I IR band of the NMA–methanol solution. We will use this two-species model for the following calculations of the 2D IR pump–probe spectra and they will be compared with those calculated by using the ensemble averaging method.

### C. Static limit

If the static (inhomogeneous) and classical limit is assumed, the absorption line shape function is simply written as

$$I(\omega)\sim\int d\mathbf{q}\,\delta(\omega-\langle\omega_{10}\rangle-\delta\omega_{10}(\mathbf{q}))\rho_0(\mathbf{q}), \tag{21}$$

where $\rho_0(\mathbf{q})$ is the equilibrium probability distribution function of bath coordinates $\mathbf{q}$. The above expression shows that the absorption line shape function is identical to the distribution of the classical variable, $\langle\omega_{10}\rangle+\delta\omega_{10}(\mathbf{q})$, which was already depicted in Fig. 3(b) (see the closed squares). Thus, in this inhomogeneous limit, though the absorption spectrum is asymmetric, it does not exhibit two separated peaks. Although, as discussed in Sec. II F, the value $\Delta_2\tau_2$ of the slowly decaying component of $M(t)$ was estimated to be 10.1, which indicates that the line-broadening induced by this slow dynamics is corresponding to the inhomogeneous limit, due to the ultrafast decaying component of $M(t)$ the line shape is significantly narrower than that in the static limit because of the motional line-narrowing process.

## IV. TWO-DIMENSIONAL IR PUMP–PROBE SPECTRA

### A. Nonlinear response functions: Ensemble averaging calculation (method 1)

In Ref. 34, the six nonlinear response functions that are directly associated with 2D IR pump–probe spectroscopy were already presented and discussed in detail. In the case of the NMA–water system, we were able to use the cumulant expansion technique to rewrite them in terms of linear lineshape function, e.g., $g(t)$.[36] However, due to the non-Gaussian nature of the amide I mode frequency fluctuation in NMA–methanol solution, one cannot directly use the same second-order cumulant-approximated expressions. Thus, in order to calculate the corresponding six nonlinear response functions denoted as $\Phi_j(t_3,t_2,t_1)$ in Ref. 36, we will use the ensemble averaging procedure used to calculate the linear response function in Sec. III. Furthermore, we will assume that $\delta\omega_{20}(t)=2\,\delta\omega_{10}(t)$. Then, we have

$$\begin{aligned}
\Phi_1(t_3,t_2,t_1)&=-|\mu_{01}|^2|\mu_{12}|^2\exp\{-i\langle\omega_{21}\rangle t_3\\
&\quad+i\langle\omega_{10}\rangle t_1\}\Psi_A(t_3,t_2,t_1)\Gamma_{\mathrm{TA}}(t_3,t_2,t_1),\\
\Phi_2(t_3,t_2,t_1)&=-|\mu_{01}|^2|\mu_{12}|^2\exp\{-i\langle\omega_{21}\rangle t_3\\
&\quad-i\langle\omega_{10}\rangle t_1\}\Psi_B(t_3,t_2,t_1)\Gamma_{\mathrm{TA}}(t_3,t_2,t_1),\\
\Phi_3(t_3,t_2,t_1)&=|\mu_{01}|^2\exp\{-i\langle\omega_{10}\rangle t_3\\
&\quad+i\langle\omega_{10}\rangle t_1\}\Psi_A(t_3,t_2,t_1)\Gamma_{\mathrm{SE}}(t_3,t_2,t_1),
\end{aligned} \tag{22}$$

$$\begin{aligned}
\Phi_4(t_3,t_2,t_1)&=|\mu_{01}|^2\exp\{-i\langle\omega_{10}\rangle t_3\\
&\quad-i\langle\omega_{10}\rangle t_1\}\Psi_B(t_3,t_2,t_1)\Gamma_{\mathrm{SE}}(t_3,t_2,t_1),\\
\Phi_5(t_3,t_2,t_1)&=|\mu_{01}|^2\exp\{-i\langle\omega_{10}\rangle t_3\\
&\quad+i\langle\omega_{10}\rangle t_1\}\Psi_A(t_3,t_2,t_1)\Gamma_{\mathrm{GB}}(t_3,t_2,t_1),\\
\Phi_6(t_3,t_2,t_1)&=|\mu_{01}|^2\exp\{-i\langle\omega_{10}\rangle t_3\\
&\quad-i\langle\omega_{10}\rangle t_1\}\Psi_B(t_3,t_2,t_1)\Gamma_{\mathrm{GB}}(t_3,t_2,t_1),
\end{aligned}$$

where the dephasing-induced line broadening factors, $\Psi_A(t_3,t_2,t_1)$ and $\Psi_B(t_3,t_2,t_1)$ are defined as

$$\begin{aligned}
\Psi_A(t_3,t_2,t_1)&\equiv\left\langle\exp\left\{i\int_0^{t_1}d\tau\,\delta\omega_{10}(\tau)\right\}\right.\\
&\quad\left.\times\exp\left\{-i\int_{t_1+t_2}^{t_1+t_2+t_3}d\tau\,\delta\omega_{10}(\tau)\right\}\right\rangle,\\
\Psi_B(t_3,t_2,t_1)&\equiv\left\langle\exp\left\{-i\int_0^{t_1}d\tau\,\delta\omega_{10}(\tau)\right\}\right.\\
&\quad\left.\times\exp\left\{-i\int_{t_1+t_2}^{t_1+t_2+t_3}d\tau\,\delta\omega_{10}(\tau)\right\}\right\rangle.
\end{aligned} \tag{23}$$

The first two contributions, $\Phi_1(t_3,t_2,t_1)$ and $\Phi_2(t_3,t_2,t_1)$, describe the transient absorption (TA) process, $\Phi_3(t_3,t_2,t_1)$ and $\Phi_4(t_3,t_2,t_1)$ are associated with the stimulated emission (SE) process where the excited state population (particle) evolution is involved, and finally $\Phi_5(t_3,t_2,t_1)$ and $\Phi_6(t_3,t_2,t_1)$ are with the ground-state bleaching (GB) contribution where a hole created on the ground state evolves in time during the population period, $t_2$. Denoting the inverse lifetimes of the first and second excited states as $\gamma_1$ and $\gamma_2$, respectively, we find that the lifetime-broadening factors in Eq. (22) are given as

$$\begin{aligned}
\Gamma_{\mathrm{TA}}(t_3,t_2,t_1)&=\exp\left\{-\frac{(\gamma_1+\gamma_2)t_3}{2}-\gamma_1t_2-\frac{\gamma_1t_1}{2}\right\},\\
\Gamma_{\mathrm{SE}}(t_3,t_2,t_1)&=\exp\left\{-\frac{\gamma_1t_3}{2}-\gamma_1t_2-\frac{\gamma_1t_1}{2}\right\},\\
\Gamma_{\mathrm{GB}}(t_3,t_2,t_1)&=\exp\left\{-\frac{\gamma_1t_3}{2}-\gamma_1t_2-\frac{\gamma_1t_1}{2}\right\}.
\end{aligned} \tag{24}$$

In order to quantitatively determine the 2D IR pump–probe spectra, the two dephasing-induced line broadening factors, $\Psi_A(t_3,t_2,t_1)$ and $\Psi_B(t_3,t_2,t_1)$, defined in Eq. (23) should be calculated from the MD trajectories.

Once these three-dimensional functions, $\Psi_A(t_3,t_2,t_1)$ and $\Psi_B(t_3,t_2,t_1)$, are determined and an impulsive pulse limit is taken, the two-dimensional IR pump–probe spectrum can be calculated as a sum of the three distinctive spectra, i.e.,

$$\begin{aligned}
S_{\mathrm{PP}}(\omega_{\mathrm{pr}},\omega_{\mathrm{pu}};\tau)\propto-\mathrm{Re}[&S_{\mathrm{TA}}(\omega_{\mathrm{pr}},\omega_{\mathrm{pu}};\tau)\\
&+S_{\mathrm{SE}}(\omega_{\mathrm{pr}},\omega_{\mathrm{pu}};\tau)\\
&+S_{\mathrm{GB}}(\omega_{\mathrm{pr}},\omega_{\mathrm{pu}};\tau)],
\end{aligned} \tag{25}$$

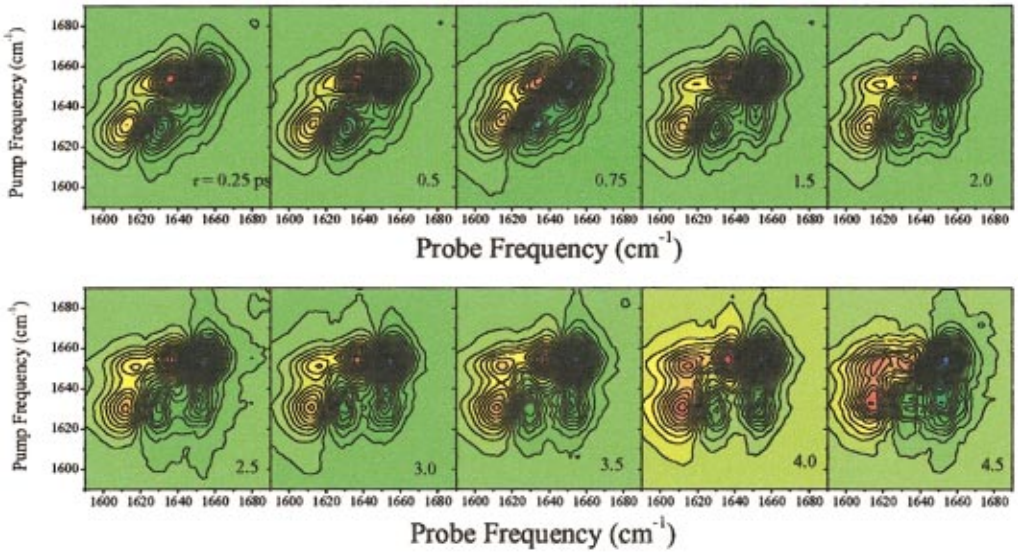


FIG. 10. (Color) Numerically calculated time-resolved 2D IR pump–probe spectra by using the ensemble averaging method.

where the three terms on the right-hand side of Eq. (25) correspond to the transient absorption, stimulated emission, and ground-state bleaching contributions, respectively, and they are

$$\Psi_{\mathrm{TA}}(\omega_{\mathrm{pr}},\omega_{\mathrm{pu}};\tau)=\tilde{\Phi}_1(\omega_{\mathrm{pr}},\omega_{\mathrm{pu}};\tau)+\tilde{\Phi}_2(\omega_{\mathrm{pr}},\omega_{\mathrm{pu}};\tau),$$

$$\Psi_{\mathrm{SE}}(\omega_{\mathrm{pr}},\omega_{\mathrm{pu}};\tau)=\tilde{\Phi}_3(\omega_{\mathrm{pr}},\omega_{\mathrm{pu}};\tau)+\tilde{\Phi}_4(\omega_{\mathrm{pr}},\omega_{\mathrm{pu}};\tau), \tag{26}$$

$$\Psi_{\mathrm{GB}}(\omega_{\mathrm{pr}},\omega_{\mathrm{pu}};\tau)=\tilde{\Phi}_5(\omega_{\mathrm{pr}},\omega_{\mathrm{pu}};\tau)+\tilde{\Phi}_6(\omega_{\mathrm{pr}},\omega_{\mathrm{pu}};\tau).$$

The pump–probe pulse delay time was denoted as $\tau$. The six 2D spectra associated with the six double-sided Feynman pathways shown in Fig. 1 of Ref. 36 are defined as

$$\tilde{\Phi}_1(\omega_{\mathrm{pr}},\omega_{\mathrm{pu}};\tau)=\int_0^\infty dt_3\int_0^\infty dt_1\exp(i\omega_{\mathrm{pr}}t_3 - i\omega_{\mathrm{pu}}t_1)\Phi_1(t_3,t_2=\tau,t_1),$$

$$\tilde{\Phi}_2(\omega_{\mathrm{pr}},\omega_{\mathrm{pu}};\tau)=\int_0^\infty dt_3\int_0^\infty dt_1\exp(i\omega_{\mathrm{pr}}t_3 + i\omega_{\mathrm{pu}}t_1)\Phi_2(t_3,t_2=\tau,t_1),$$

$$\tilde{\Phi}_3(\omega_{\mathrm{pr}},\omega_{\mathrm{pu}};\tau)=\int_0^\infty dt_3\int_0^\infty dt_1\exp(i\omega_{\mathrm{pr}}t_3 - i\omega_{\mathrm{pu}}t_1)\Phi_3(t_3,t_2=\tau,t_1),$$

$$\tilde{\Phi}_4(\omega_{\mathrm{pr}},\omega_{\mathrm{pu}};\tau)=\int_0^\infty dt_3\int_0^\infty dt_1\exp(i\omega_{\mathrm{pr}}t_3 + i\omega_{\mathrm{pu}}t_1)\Phi_4(t_3,t_2=\tau,t_1), \tag{27}$$

$$\tilde{\Phi}_5(\omega_{\mathrm{pr}},\omega_{\mathrm{pu}};\tau)=\int_0^\infty dt_3\int_0^\infty dt_1\exp(i\omega_{\mathrm{pr}}t_3 - i\omega_{\mathrm{pu}}t_1)\Phi_5(t_3,t_2=\tau,t_1),$$

$$\tilde{\Phi}_6(\omega_{\mathrm{pr}},\omega_{\mathrm{pu}};\tau)=\int_0^\infty dt_3\int_0^\infty dt_1\exp(i\omega_{\mathrm{pr}}t_3 + i\omega_{\mathrm{pu}}t_1)\Phi_6(t_3,t_2=\tau,t_1).$$

### B. Numerically calculated 2D IR pump–probe spectra

Directly calculating the dephasing-induced line broadening functions, $\Psi_A(t_3,t_2,t_1)$ and $\Psi_B(t_3,t_2,t_1)$, with MD simulation results, we obtained *time-resolved* 2D IR pump–probe spectra and plotted them in Fig. 10. Here, we assumed that the lifetime of the second excited state, $1/\gamma_2$, is assumed to be 0.9 ps—note that $1/\gamma_1$ was put to be 1.8 ps in the calculation of the IR absorption spectra. It should be emphasized that the lifetimes of the two species can be different from each other as was mentioned by Woutersen *et al.* in Ref. 39. However, in the present study we were not able to take into account this difference properly, as long as the ensemble averaging method is directly used to quantitatively calculate the nonlinear response functions. This is because the lifetime relaxation effect could not be taken into account in the MD trajectory calculation. However, as will be discussed in the following subsections, if the two-species model is used one can treat the different lifetime-broadening effects on the nonlinear response functions associated with various reaction pathways.

### C. Off-diagonal cross peaks: Ensemble averaged 2D spectra

In Fig. 10, in addition to the decaying two diagonal peaks that are associated with the two peaks in the 1D IR absorption band, there appear two off-diagonal cross peaks at ($\omega_{\mathrm{pu}}=1632$, $\omega_{\mathrm{pr}}=1650$) and ($\omega_{\mathrm{pu}}=1650$, $\omega_{\mathrm{pr}}=1615$) of which relative intensities increase as the pump–probe pulse delay time increases. This was experimentally observed by Woutersen *et al.*[39] In Fig. 11, we plot the time-resolved sliced spectra at two different pump frequencies, 1632 and

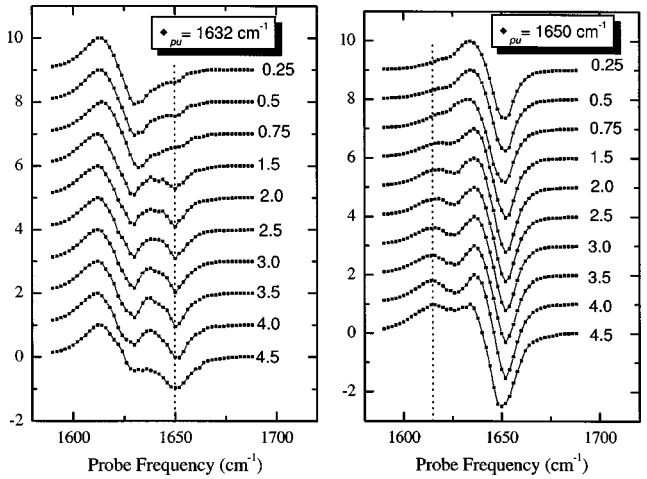


FIG. 11. The time-resolved sliced spectra at two different pump frequencies, 1632 and 1650 $cm^{-1}$, obtained from the results of Fig. 10.

1650 $cm^{-1}$, which correspond to the two center frequencies of the IR absorption peaks. The dip at $\omega_{pr}=1650\,cm^{-1}$ when the pump field frequency is 1632 $cm^{-1}$ is getting deeper as the delay time increases, whereas the intensity of the cross peak at $\omega_{pr}=1615\,cm^{-1}$ when the pump field frequency is 1650 $cm^{-1}$ increases. The physical meaning of these cross peaks is the following. For instance, let us consider the cross peak at ($\omega_{pu}=1632$, $\omega_{pr}=1650$). The pump field of which frequency is 1632 $cm^{-1}$ interacts with the $NM_2$ species at time $t\approx 0$ so that an amide I vibrational coherence state of the $NM_2$ is created initially. Then, as the delay time increases, the species $NM_2$ undergoes a conformational transition to $NM_1$ by the dissociation of a single MeOH molecule among the two of $NM_2$. Thus, at time $\tau$ later, the population of $NM_1$ that is a product of the backward reaction from $NM_2$ to $NM_1$ increases, which appears as a growth of this cross peak intensity. In this case, the peak intensity rise is directly associated with the forward and backward rate constants. More specifically, the time evolution of this cross peak is dictated by the conditional probability of finding $NM_1$ at time $\tau$ when the solvation configuration was $NM_2$ at time zero. Similarly, the cross peak intensity change in the spectral region around ($\omega_{pu}=1650$, $\omega_{pr}=1615$) can be interpreted, though the intensity change in this case is related to the conformation transition from $NM_1$ to $NM_2$, where an additional formation of an H-bond with NMA and a second MeOH molecule is involved.

Although we have observed and described the temporal evolutions of the two cross peaks, there is a lack of microscopic and quantitative descriptions in terms of the rate constants. In the following subsection, using the two-species model with kinetics analysis result presented in Sec. II D, we will quantitatively predict the time evolution of 2D IR pump–probe spectra.

### D. Two-species model description of 2D IR pump–probe spectra

Essentially there are four distinctively different chemical reaction pathways that are relevant to the 2D IR pump–probe spectroscopy of the NMA–methanol solution. They are

$$\text{Pathway 1:}\quad \mathrm{NM}_1(\tau=0)\rightarrow \mathrm{NM}_1(\tau=\tau),$$
$$\text{Pathway 2:}\quad \mathrm{NM}_2(\tau=0)\rightarrow \mathrm{NM}_2(\tau=\tau),$$
$$\text{Pathway 3:}\quad \mathrm{NM}_1(\tau=0)\rightarrow \mathrm{NM}_2(\tau=\tau),$$
$$\text{Pathway 4:}\quad \mathrm{NM}_2(\tau=0)\rightarrow \mathrm{NM}_1(\tau=\tau).$$

As briefly mentioned in the above subsection, the two pathways 3 and 4 are associated with the cross peaks at ($\omega_{pu}=1650$, $\omega_{pr}=1615$) and ($\omega_{pu}=1632$, $\omega_{pr}=1650$), respectively, whereas the first two pathways 1 and 2 are with the two diagonal peaks at ($\omega_{pu}=1650$, $\omega_{pr}=1650$) and ($\omega_{pu}=1632$, $\omega_{pr}=1632$), respectively. Taking into account these four different reaction pathways contributing to the 2D IR pump–probe signal, we can write down the total 2D spectrum as

$$\begin{aligned} S_{\mathrm{PP}}(\omega_{\mathrm{pr}},\omega_{\mathrm{pu}};\tau) &= G_{\mathrm{NM}_1\rightarrow\mathrm{NM}_1}(\tau)S_{\mathrm{NM}_1\rightarrow\mathrm{NM}_1}(\omega_{\mathrm{pr}},\omega_{\mathrm{pu}};\tau) \\ &+ G_{\mathrm{NM}_2\rightarrow\mathrm{NM}_2}(\tau)S_{\mathrm{NM}_2\rightarrow\mathrm{NM}_2}(\omega_{\mathrm{pr}},\omega_{\mathrm{pu}};\tau) \\ &+ G_{\mathrm{NM}_1\rightarrow\mathrm{NM}_2}(\tau)S_{\mathrm{NM}_1\rightarrow\mathrm{NM}_2}(\omega_{\mathrm{pr}},\omega_{\mathrm{pu}};\tau) \\ &+ G_{\mathrm{NM}_2\rightarrow\mathrm{NM}_1}(\tau)S_{\mathrm{NM}_2\rightarrow\mathrm{NM}_1}(\omega_{\mathrm{pr}},\omega_{\mathrm{pu}};\tau), \end{aligned} \tag{28}$$

where, for example, the conditional probability of finding $NM_2$ at time $\tau$ when it was initially in the $NM_1$ configuration at time zero was denoted as $G_{\mathrm{NM}_1\rightarrow\mathrm{NM}_2}(\tau)$. The four conditional probability functions can be obtained from the rate equation in (5) and are given as

$$\begin{aligned} G_{\mathrm{NM}_1\rightarrow\mathrm{NM}_1}(\tau) &= X_{\mathrm{NM}_1}\frac{k_b+k_f e^{-(k_f+k_b)\tau}}{k_f+k_b}, \\ G_{\mathrm{NM}_2\rightarrow\mathrm{NM}_2}(\tau) &= X_{\mathrm{NM}_2}\frac{k_f+k_b e^{-(k_f+k_b)\tau}}{k_f+k_b}, \\ G_{\mathrm{NM}_1\rightarrow\mathrm{NM}_2}(\tau) &= X_{\mathrm{NM}_1}\frac{k_f-k_f e^{-(k_f+k_b)\tau}}{k_f+k_b}, \\ G_{\mathrm{NM}_2\rightarrow\mathrm{NM}_1}(\tau) &= X_{\mathrm{NM}_2}\frac{k_b-k_b e^{-(k_f+k_b)\tau}}{k_f+k_b}. \end{aligned} \tag{29}$$

The two time-dependent 2D spectra, $S_{\mathrm{NM}_1\rightarrow\mathrm{NM}_1}(\omega_{\mathrm{pr}},\omega_{\mathrm{pu}};\tau)$ and $S_{\mathrm{NM}_2\rightarrow\mathrm{NM}_2}(\omega_{\mathrm{pr}},\omega_{\mathrm{pu}};\tau)$, can be calculated by following the same procedure presented in Ref. 36 since in these cases one can use the cumulant expansion expressions for the corresponding nonlinear response functions—note that each of the fluctuating amide I mode frequency distributions of $NM_1$ and $NM_2$ is a perfect Gaussian function. Here, it should be noted that during the delay time $\tau$ any of the two species can undergo arbitrary number of conformational transitions between $NM_1$ and $NM_2$, which in turn will induce additional dephasing process. However, this conformational-transition-induced dephasing was taken into account by the conditional probability functions, $G_{\mathrm{NM}_1\rightarrow\mathrm{NM}_1}(\tau)$ and $G_{\mathrm{NM}_2\rightarrow\mathrm{NM}_2}(\tau)$ approximately.

We next present a theoretical description on how to calculate $S_{\mathrm{NM}_1\rightarrow\mathrm{NM}_2}(\omega_{\mathrm{pr}},\omega_{\mathrm{pu}};\tau)$ and $S_{\mathrm{NM}_2\rightarrow\mathrm{NM}_1}(\omega_{\mathrm{pr}},\omega_{\mathrm{pu}};\tau)$ that are associated with the two cross peaks at ($\omega_{pu}=1650$,

$\omega_{pr}=1650$) and ($\omega_{pu}=1632$, $\omega_{pr}=1632$), respectively. In order to obtain analytical expressions for the corresponding nonlinear response functions, it will be necessary to treat the chemical reaction (conformational transitions between $NM_1$ and $NM_2$) microscopically. Let us consider the case of pathway 3, i.e., $NM_1 \rightarrow NM_2$. The initial vibrational coherence of $NM_1$ at time zero, which is created by the pump field–$NM_1$ interaction, can be in correlation with that of $NM_2$ at time $\tau$ when $NM_2$ interacts with the probe field. One can consider two limiting cases; (1) perfect correlation limit, where the vibrational phase of the initial coherence state of the $NM_1$ species is perfectly preserved during $\tau$ and (2) no correlation limit, where the conformational transition (or transitions) of $NM_1 \rightarrow NM_2$ completely destroys any memory (or correlation) on the initial vibrational phase. There is a possibility that the real situation is just in between these two limits. However, when we calculated the absorption line shape by using the two-species model, we already invoked an approximation that the entire phase space can be divided into two spaces of $NM_1$ and $NM_2$. This approximation implies that the vibrational phase information is completely lost when the system undergoes a conformational transition between the two species. Within this approximation, the numerically calculated $I(\omega)$ in Fig. 9(b) appeared to be in a quantitative agreement with that calculated by using the ensemble averaging method that is not relied on the above approximation. Then, in order to calculate nonlinear response functions associated with $S_{NM_1\rightarrow NM_2}(\omega_{pr},\omega_{pu};\tau)$ and $S_{NM_2\rightarrow NM_1}(\omega_{pr},\omega_{pu};\tau)$, one can rewrite the classical ensemble averaging integral over the entire phase space as a product of two ensemble averaging integrals over the $NM_1$ and $NM_2$ phase spaces. To be more specific, the ensemble average expression for $\Psi_A^{NM_1\rightarrow NM_2}(t_3,t_2,t_1)$ that is associated with the $S_{NM_1\rightarrow NM_2}(\omega_{pr},\omega_{pu};\tau)$ is approximated as

$$\begin{aligned}\Psi_A^{NM_1\rightarrow NM_2}(t_3,t_2,t_1)&=\left\langle \exp\left\{ i\int_0^{t_1} d\tau\,\delta\omega_{10}(\tau)\right\}\exp\left\{ -i\int_{t_1+t_2}^{t_1+t_2+t_3} d\tau\,\delta\omega_{10}(\tau)\right\}\right\rangle\\ &\cong\left\langle \exp\left\{ i\int_0^{t_1} d\tau\,\delta\omega_{10}(\tau)\right\}\right\rangle_{NM_1}\left\langle \exp\left\{ -i\int_0^{t_3} d\tau\,\delta\omega_{10}(\tau)\right\}\right\rangle_{NM_2}\\ &\cong\exp\{-g_1(t_1)-g_2(t_3)\},\end{aligned}\tag{30}$$

where the last equality was obtained by using the second-order cumulant expansion method and the imaginary part of $g(t)$, which is associated with spectral diffusion, was ignored because they are negligibly small as was the case of the NMA–water system.[36] In this limit, one can prove that $\Psi_A^{NM_1\rightarrow NM_2}(t_3,t_2,t_1)=\Psi_B^{NM_1\rightarrow NM_2}(t_3,t_2,t_1)$. Then, the six nonlinear response function components, which are associated with $S_{NM_1\rightarrow NM_2}(\omega_{pr},\omega_{pu};\tau)$, are found to be

$$\begin{aligned}\Phi_1^{NM_1\rightarrow NM_2}(t_3,t_2,t_1)&=-|\mu_{01}|^2|\mu_{12}|^2\exp\{-i\langle\omega_{21}\rangle_{NM_2}t_3+i\langle\omega_{10}\rangle_{NM_1}t_1\}\exp\{-g_1(t_1)-g_2(t_3)\}\Gamma_{TA}^{NM_1\rightarrow NM_2}(t_3,t_2,t_1),\\ \Phi_2^{NM_1\rightarrow NM_2}(t_3,t_2,t_1)&=-|\mu_{01}|^2|\mu_{12}|^2\exp\{-i\langle\omega_{21}\rangle_{NM_2}t_3-i\langle\omega_{10}\rangle_{NM_1}t_1\}\exp\{-g_1(t_1)-g_2(t_3)\}\Gamma_{TA}^{NM_1\rightarrow NM_2}(t_3,t_2,t_1),\\ \Phi_3^{NM_1\rightarrow NM_2}(t_3,t_2,t_1)&=-|\mu_{01}|^2\exp\{-i\langle\omega_{10}\rangle_{NM_2}t_3+i\langle\omega_{10}\rangle_{NM_1}t_1\}\exp\{-g_1(t_1)-g_2(t_3)\}\Gamma_{SE}^{NM_1\rightarrow NM_2}(t_3,t_2,t_1),\\ \Phi_4^{NM_1\rightarrow NM_2}(t_3,t_2,t_1)&=-|\mu_{01}|^2\exp\{-i\langle\omega_{10}\rangle_{NM_2}t_3-i\langle\omega_{10}\rangle_{NM_1}t_1\}\exp\{-g_1(t_1)-g_2(t_3)\}\Gamma_{SE}^{NM_1\rightarrow NM_2}(t_3,t_2,t_1),\\ \Phi_5^{NM_1\rightarrow NM_2}(t_3,t_2,t_1)&=-|\mu_{01}|^2\exp\{-i\langle\omega_{10}\rangle_{NM_2}t_3+i\langle\omega_{10}\rangle_{NM_1}t_1\}\exp\{-g_1(t_1)-g_2(t_3)\}\Gamma_{GB}^{NM_1\rightarrow NM_2}(t_3,t_2,t_1),\\ \Phi_6^{NM_1\rightarrow NM_2}(t_3,t_2,t_1)&=-|\mu_{01}|^2\exp\{-i\langle\omega_{10}\rangle_{NM_2}t_3-i\langle\omega_{10}\rangle_{NM_1}t_1\}\exp\{-g_1(t_1)-g_2(t_3)\}\Gamma_{GB}^{NM_1\rightarrow NM_2}(t_3,t_2,t_1),\end{aligned}\tag{31}$$

where

$$\begin{aligned}\Gamma_{TA}^{NM_1\rightarrow NM_2}(t_3,t_2,t_1)&=\exp\left\{-\frac{(\gamma_1^{NM_2}+\gamma_2^{NM_2})t_3}{2}-\frac{(\gamma_1^{NM_1}+\gamma_1^{NM_2})}{2}t_2-\frac{\gamma_1^{NM_1}t_1}{2}\right\},\\ \Gamma_{SE}(t_3,t_2,t_1)&=\exp\left\{-\frac{\gamma_1^{NM_2}t_3}{2}-\frac{(\gamma_1^{NM_1}+\gamma_1^{NM_2})}{2}t_2-\frac{\gamma_1^{NM_1}t_1}{2}\right\},\\ \Gamma_{GB}(t_3,t_2,t_1)&=\exp\left\{-\frac{\gamma_1^{NM_2}t_3}{2}-\frac{(\gamma_1^{NM_1}+\gamma_1^{NM_2})}{2}t_2-\frac{\gamma_1^{NM_1}t_1}{2}\right\}.\end{aligned}\tag{32}$$

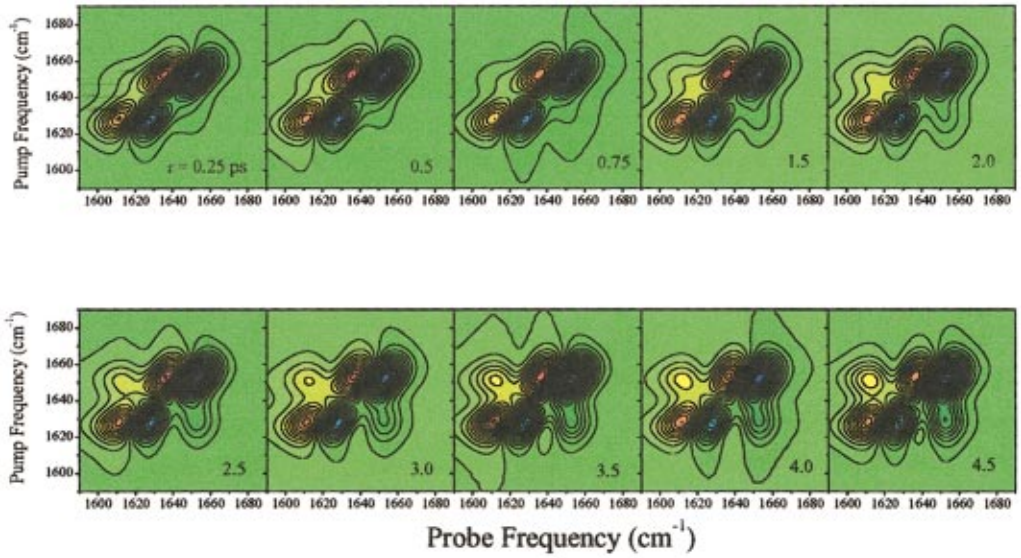


FIG. 12. (Color) Time-resolved 2D IR pump–probe spectra obtained by using the two-species model.

Here, the lifetimes of the first excited states of $NM_1$ and $NM_2$ were denoted as $\gamma_1^{NM_1}$ and $\gamma_1^{NM_2}$, respectively, and those of the second excited states of $NM_1$ and $NM_2$ were as $\gamma_2^{NM_1}$ and $\gamma_2^{NM_2}$, respectively. We assumed that the lifetime contribution to the dephasing during the population period, $t_2=\tau$, was described by the average lifetime constant, $(\gamma_1^{NM_1}+\gamma_1^{NM_2})/2$, which will be assumed to be 1.8 ps. Note that the above theory is general enough to take into account the aspect that the lifetimes of the two species can be different from each other.

The nonlinear response functions, $\Phi_j^{NM_1\rightarrow NM_2}(t_3,t_2,t_1)$ (for $j=1-6$), associated with $S_{NM_2\rightarrow NM_1}(\omega_{pr},\omega_{pu};\tau)$, which is the fourth term in Eq. (28), can be obtained by making the following replacements:

$$
\begin{aligned}
&\langle\omega_{21}\rangle_{NM_2}t_3\rightarrow\langle\omega_{21}\rangle_{NM_1}t_3,\\
&\langle\omega_{10}\rangle_{NM_2}t_3\rightarrow\langle\omega_{10}\rangle_{NM_1}t_3,\\
&\langle\omega_{10}\rangle_{NM_1}t_1\rightarrow\langle\omega_{10}\rangle_{NM_2}t_1,\\
&g_1(t_1)\rightarrow g_2(t_1),\\
&g_2(t_3)\rightarrow g_1(t_3),\\
&\gamma_1^{NM_1}t_1\rightarrow\gamma_1^{NM_2}t_1,\\
&(\gamma_1^{NM_2}+\gamma_2^{NM_2})t_3\rightarrow(\gamma_1^{NM_1}+\gamma_2^{NM_1})t_3,\\
&\gamma_1^{NM_2}t_3\rightarrow\gamma_1^{NM_1}t_3.
\end{aligned}
\tag{33}
$$

### E. Numerical simulation of the 2D IR pump–probe spectra using the two-species model description

We now numerically calculate the time-resolved 2D spectra by using the above two-species model, and they are plotted in Fig. 12 and are in quantitative agreement with those in Fig. 10 obtained with the ensemble averaging method. The intensities of the two cross peaks increase as the delay time $\tau$ increases, as expected. Although each of the two cross peaks is not a single peak but two separated (positive and negative) peaks due to the anharmonicity of the amide I oscillator much like the two diagonal peaks, due to the destructive interference only two cross peaks, a positive peak at ($\omega_{pu}=1650$, $\omega_{pr}=1615$) and a negative peak at ($\omega_{pu}=1632$, $\omega_{pr}=1650$) are notable. That is to say, the other two cross peaks at ($\omega_{pu}=1650$, $\omega_{pr}=1632$) and ($\omega_{pu}=1632$, $\omega_{pr}=1636$) originated from the conformational transitions from $NM_1$ to $NM_2$ and from $NM_2$ to $NM_1$, respectively, are not shown up distinctively because their intensities are largely cancelled out when they are added to the diagonal peaks.

The two-species model with theoretical descriptions presented above was found to be successful in quantitatively describing the effects of H-bonding dynamics on the 2D line shapes of time-resolved pump–probe spectra. However, the current theoretical model needs to be farther developed in the future. First of all, if the no-correlation-approximation mentioned in Sec. IV D is invoked to describe the 2D line shapes of cross peaks [see Eq. (31)], their 2D contours will appear to be vertically directed all the time. This prediction seems to be reasonable because those cross peaks in Fig. 10 have no discernable slant features. However, the contours of two diagonal peaks (see Fig. 12) are not vertically directed even at time $\tau=4.5$ ps. On the other hand, the two contours of diagonal peaks in Fig. 10 are vertically directed after $\tau$ larger than 3.5 ps. There are two possible explanations for this. Recently, Kwac and Cho showed that the inverse slope of the tilted contours is linearly proportional to the solvation dynamics and its magnitude is a signature that the initial vibrational phase memory survives over the population evolution period.[37] If there is a static inhomogeneity, the asymptotic value of the inverse slope does not approach zero. On the basis of this theory, the tilted 2D contours of the two diagonal peaks in Fig. 12 originate from the long-time asymptotic values of $M_1(t)$ and $M_2(t)$. However, there is a possibility that the slowly decaying components (or long-time values)

of $M_1(t)$ and $M_2(t)$ are just an artifact due to the insufficient ensemble averaging. Note that the average lifetimes of $NM_1$ and $NM_2$ species are a few or tens of picoseconds so that the ensemble averages were calculated over those short segments of MD trajectories. Particularly, the lifetime of the $NM_2$ is shorter than that of $NM_1$ so that the quality of statistical average is relatively poor as can be seen in the long-time (>2 ps) part of $M_2(t)$. The second possibility is that the theoretical model used to calculate the two diagonal peaks is not accurate enough to describe the additional memory-loss process induced by the conformational transitions during $\tau$. The temporal evolution of the tilting angles of 2D contours in Fig. 10 suggests that an additional process, associated with the conformational transitions between the two species, increases the (phase of the amide I vibrational coherence state) memory loss rate during $\tau$.

## V. SUMMARY AND A FEW CONCLUDING REMARKS

In the present paper, we carried out MD simulation, in combination with *ab initio* calculations of NMA$-(CH_3OH)_n$ clusters, and presented theoretical descriptions of linear and nonlinear vibrational spectroscopies of an NMA dissolved in liquid methanol. Unlike an aqueous NMA solution, the distribution of the fluctuating amide I mode frequency is non-Gaussian, which was found to originate from the existence of two different solvation structures, denoted as $NM_1$ and $NM_2$ in the present paper. Due to the non-Gaussian statistics of the amide I frequency fluctuation, the well-known second-order cumulant expansion method could not be used to calculate linear and nonlinear vibrational response functions. Therefore, we directly calculated them by using the so-called ensemble averaging method and thus calculated IR absorption and 2D IR pump–probe spectra were found to be in an excellent agreement with experimental results. Treating the interconversion process between $NM_1$ and $NM_2$ as an equilibrium reaction and using the Onsager's regression hypothesis,[50] we determined the two rate constants, which were then used to theoretically describe the time-evolution of the 2D IR pump–probe spectra. In particular, the cross-peak intensity changes that reflect the ultrafast reaction dynamics between $NM_1$ and $NM_2$ species were successfully explained by the theory presented in this paper. This suggests that the 2D IR pump–probe spectroscopy can be of use to study ultrafast and *coherent* chemical reactions without relying on conventional relaxation methods, such as temperature-jump, pressure-jump, etc.

In order to quantitatively describe the time evolution of the cross-peak intensity, we assumed that the memory on the vibrational coherence created by the pump field-chromophore interaction is completely lost if the species undergoes a conformational transition from $NM_1$ to $NM_2$ or vice versa. Within this approximation, the 2D line shape of the cross peak is vertically directed all the time because the nonlinear response function was approximately written as a product of two linear response functions [see Eq. (31)]. However, in reality the vibrational phase memory can survive over the chemical reaction process and in this case the time-dependent 2D line shapes of the diagonal and cross peaks would carry the information on the coherence transfer over the chemical reaction. Currently, we are developing a theory on this aspect and will present the result elsewhere.

## ACKNOWLEDGMENT

This work was supported by the Creative Research Initiatives Program of KISTEP (MOST, Korea).

[1] S. Krimm and J. Bandekar, Adv. Protein Chem. **38**, 181 (1986).
[2] *Infrared Spectroscopy of Biomolecules*, edited by H. H. Mantsch and D. Chapman (Wiley–Liss, New York, 1996).
[3] *Infrared and Raman Spectroscopy of Biological Materials*, edited by H.-U. Gremlich and B. Yan (Dekker, New York, 2001).
[4] G. Sieler and R. Schweitzer-Stenner, J. Am. Chem. Soc. **119**, 1720 (1997).
[5] G. Mix, R. Schweitzer-Stenner, and S. A. Asher, J. Am. Chem. Soc. **122**, 9028 (2000).
[6] R. Schweitzer-Stenner, Biophys. J. **83**, 523 (2002).
[7] F. Eker, X. Cao, L. Nafie, and R. Schweitzer-Stenner, J. Am. Chem. Soc. **124**, 14330 (2002); J. Phys. Chem. B **107**, 358 (2003).
[8] J. Kubelka and T. A. Keiderling, J. Phys. Chem. A **105**, 10922 (2001); J. Am. Chem. Soc. **123**, 6142 (2001); **123**, 12048 (2001).
[9] J.-H. Choi, S. Ham, and M. Cho, J. Phys. Chem. B **107**, 9132 (2003).
[10] S. Ham, S. Cha, J.-H. Choi, and M. Cho, J. Chem. Phys. **119**, 1451 (2003).
[11] E. S. Manas, Z. Getahun, W. W. Wright, W. F. DeGrado, and J. M. Vanderkooi, J. Am. Chem. Soc. **122**, 9883 (2000).
[12] S. K. Gregurick, E. Fredj, R. Elber, and R. B. Gerber, J. Phys. Chem. B **101**, 8595 (1997).
[13] S. M. Decatur, Biopolymers **54**, 180 (2000).
[14] J. Torres and E. Padros, Biophys. J. **68**, 2049 (1995).
[15] H. Susi and D. M. Byler, Biochem. Biophys. Res. Commun. **115**, 391 (1983).
[16] J. W. Brauner, C. Dugan, and R. Mendelsohn, J. Am. Chem. Soc. **122**, 677 (2000).
[17] H. Torri and M. Tasumi, J. Chem. Phys. **96**, 3379 (1992).
[18] A. Y. Chikishev, G. W. Lucassen, N. I. Koroteev, C. Otto, and J. Greve, Biophys. J. **63**, 976 (1992).
[19] P. Hamm, M. Lim, and R. M. Hochstrasser, J. Phys. Chem. B **102**, 6123 (1998).
[20] P. Hamm, M. Lim, W. F. DeGrado, and R. M. Hochstrasser, Proc. Natl. Acad. Sci. U.S.A. **96**, 2036 (1999); J. Phys. Chem. A **103**, 10049 (1999); J. Chem. Phys. **112**, 1907 (2000).
[21] S. Woutersen and P. Hamm, J. Phys. Chem. B **104**, 11316 (2000); J. Chem. Phys. **114**, 2727 (2001); **115**, 7737 (2001).
[22] S. Woutersen, Y. Mu, G. Stock, and P. Hamm, Proc. Natl. Acad. Sci. U.S.A. **98**, 11254 (2001).
[23] S. Woutersen, R. Pfister, P. Hamm, Y. Mu, D. S. Kosov, and G. Stock, J. Chem. Phys. **117**, 6833 (2002).
[24] J. Brendenbeck, J. Helbing, R. Behrendt, C. Renner, L. Moroder, J. Wachtveitl, and P. Hamm, J. Phys. Chem. B **107**, 8654 (2003).
[25] M. T. Zanni, S. Gnanakaran, Jens Stenger, and R. M. Hochstrasser, J. Phys. Chem. B **105**, 6520 (2001).
[26] S. Gnanakaran and R. M. Hochstrasser, J. Am. Chem. Soc. **123**, 12886 (2001).
[27] I. V. Rubtsov and R. M. Hochstrasser, J. Phys. Chem. B **106**, 9165 (2002).
[28] A. Piryatinski, S. Tretiak, V. Chernyak, and S. Mukamel, J. Raman Spectrosc. **31**, 125 (2000).
[29] C. Scheurer, A. Piryatinski, and S. Mukamel, J. Am. Chem. Soc. **123**, 3114 (2001).
[30] A. M. Moran, S.-M. Park, J. Dreyer, and S. Mukamel, J. Chem. Phys. **118**, 3651 (2003).
[31] A. T. Krummel, P. Mukherjee, and M. T. Zanni, J. Phys. Chem. B **107**, 9165 (2003).
[32] M. Cho, *Advances in Multiphoton Processes and Spectroscopy*, edited by S. H. Lin, A. A. Villaeys, and Y. Fujimura (World Scientific, Singapore, 1999), Vol. 12, p. 229.
[33] M. Cho, PhysChemComm **5**, 40 (2002).
[34] M. Cho, J. Chem. Phys. **115**, 4424 (2001).
[35] M. Khalil, N. Demirdoven, and A. Tokmakoff, J. Phys. Chem. A **107**, 5258 (2003); Phys. Rev. Lett. **90**, 047401 (2003).
[36] K. Kwac and M. Cho, J. Chem. Phys. **119**, 2256 (2003).
[37] K. Kwac and M. Cho, J. Phys. Chem. A **107**, 5903 (2003).
[38] M. T. Zanni, M. C. Asplund, and R. M. Hochstrasser, J. Chem. Phys. **114**, 4579 (2001).

[39] S. Woutersen, Y. Mu, G. Stock, and P. Hamm, Chem. Phys. **266**, 137 (2001).
[40] G. Eaton, M. C. R. Symons, and P. P. Rastogi, J. Chem. Soc., Faraday Trans. 1 **85**, 3257 (1989).
[41] S. Ham, J.-H. Kim, H. Lee, and M. Cho, J. Chem. Phys. **118**, 3491 (2003).
[42] M. Cho, J. Chem. Phys. **118**, 3480 (2003).
[43] K. Kwac and M. Cho, J. Chem. Phys. **119**, 2247 (2003).
[44] M. J. Frisch, G. W. Trucks, H. B. Schlegel *et al.*, GAUSSIAN 98, Revision A.7, Gaussian, Inc., Pittsburgh, Pennsylvania, 1998.
[45] D. A. Case, D. A. Pearlman, J. W. Caldwell *et al.*, AMBER 7 (University of California, San Francisco, 2002). For a detailed discussion on the force field parameters, parm99, the following papers should be referred to: W. D. Cornell, P. Cieplak, C. I. Bayly, I. R. Gould, K. M. Merz, Jr., D. M. Ferguson, D. C. Spellmeyer, T. Fox, J. W. Caldwell, and P. A. Kollman, J. Am. Chem. Soc. **117**, 5179 (1995); T. E. Cheatham III, P. Cieplak, and P. A. Kollman, J. Biomol. Struct. Dyn. **16**, 845 (1999); C. I. Bayly, P. Cieplak, W. D. Cornell, and P. A. Kollman, J. Phys. Chem. **97**, 10269 (1993); W. D. Cornell, P. Cieplak, C. I. Bayly, and P. A. Kollman, J. Am. Chem. Soc. **115**, 9620 (1993); P. Cieplak, W. D. Cornell, C. Bayly, and P. A. Kollman, J. Comput. Chem. **16**, 1357 (1995); A. St.-Amant, W. D. Cornell, P. A. Kollman, and T. A. Halgren, *ibid.* **16**, 1483 (1995).
[46] T. Darden, D. York, and L. Pedersen, J. Chem. Phys. **98**, 10089 (1993).
[47] H. J. C. Berendsen, J. P. M. Postma, W. F. van Gunsteren, A. DiNola, and J. R. Haak, J. Chem. Phys. **81**, 3684 (1984).
[48] MD simulation method and force field used in the present paper differ from those used by Woutersen *et al.* in Ref. 39. First of all, the AMBER program with parm99 force field was used in this work, whereas they used the GROMOS program with force field 43Al. However, since the NMA is a relatively rigid molecule unlike other polypeptide molecules, these differences in MD packages and force fields may not induce any notable difference. Secondly, we used no coupling scheme in the production run after the equilibration run at 298 K so that our MD was performed in the NVE condition. On the other hand, they employed the pressure and temperature couplings so that their simulation corresponds to the isothermal–isobaric ensemble. Nevertheless, it is believed that this should not be the reason why their conclusion differs from ours as to the number of H-bonded methanol molecules to the C═O group of the NMA. Thirdly, they used the SHAKE algorithm and their MD time step was 2 fs, whereas we did not use the SHAKE algorithm and our MD time step was 0.5 fs. The latter difference in simulation method is likely to be the reason. Furthermore, the quantum chemistry calculation studies of NMA–methanol clusters, which was presented in Sec. II A, support that the C═O group of the NMA can form two H-bonds with methanol molecules, similar to the cases of NMA–water clusters discussed in Ref. 41.
[49] S. Mukamel, *Principles of Nonlinear Optical Spectroscopy* (Oxford University Press, Oxford, 1995).
[50] D. Chandler, *Introduction to Modern Statistical Mechanics* (Oxford University Press, Oxford, 1987).
[51] D. A. McQuarrie, *Statistical Mechanics* (Harper Collins, New York, 1976).
[52] J. R. Schmidt, N. Sundlass, and J. L. Skinner, Chem. Phys. Lett. **378**, 559 (2003).